Materials and Design 164 (2019) 107561

Contents lists available at ScienceDirect

Materials and Design

journal homepage: www.elsevier.com/locate/matdes

# Ultrasound freeze casting: Fabricating bioinspired porous scaffolds through combining freeze casting and ultrasound directed self-assembly

Taylor A. Ogden, Milo Prisbrey, Isaac Nelson, Bart Raeymaekers, Steven E. Naleway *

*University of Utah, Department of Mechanical Engineering, United States of America*

## HIGHLIGHTS

- We combine titania-based freeze casting with ultrasound directed self-assembly in a new process: ultrasound freeze casting.
- Altering the applied operating frequency from 0-936 kHz creates structures of 3-5 dense and porous concentric rings.
- The dense and porous rings display significant changes in Vickers hardness (19.37HV-24.52HV) and porosity (37.08%-21.73%).

## GRAPHICAL ABSTRACT

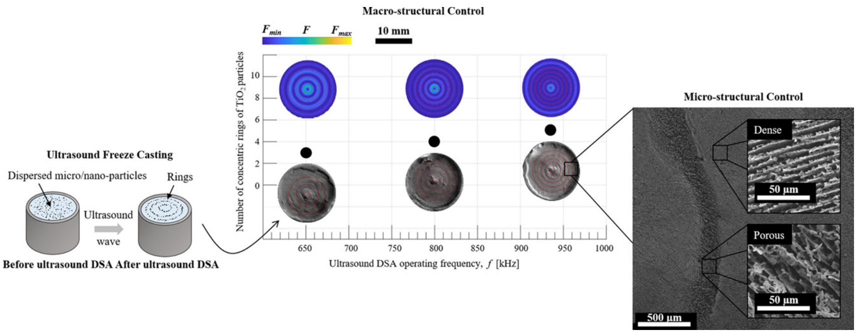

## ARTICLE INFO

*Article history:*
Received 6 September 2018
Received in revised form 20 December 2018
Accepted 20 December 2018
Available online 22 December 2018

*Keywords:*
Freeze casting
Ultrasound directed self-assembly
Bioinspired
Mechanical properties

## ABSTRACT

Lightweight porous engineered materials are advantageous in a broad range of research fields because they combine desirable mechanical properties with the ability to leverage their porous structure. Existing techniques for fabricating porous material structures are limited by material choice, require multiple steps, and/or additional post-processing to create regions of varying material properties within the material structure, and are not easily scalable. In contrast, we implement and characterize a fabrication process for macroscale porous engineered material samples with a user-specified microstructure, by combining freeze casting, which allows fabrication of porous materials samples, with ultrasound directed self-assembly, which allows controlling the microstructure of the porous materials. We refer to this process as "ultrasound freeze casting (UFC)," and employ it to fabricate bioinspired materials that mimic the concentric rings of natural materials such as osteons and Liesegang rings. Specifically, we employ the UFC process to create material samples with three, four, and five concentric rings of alternating dense and porous $TiO_2$ material. We find statistically significant differences of both the porosity and Vickers hardness when comparing the porous and dense regions of the material samples. These results will provide a new pathway to fabricate porous engineered materials with user-specified microstructure.

## 1. Introduction

Lightweight porous engineered materials are advantageous in a broad range of research fields because they combine desirable mechanical properties, such as a high strength-to-weight ratio, with the ability to leverage its porous structure for e.g., fluid storage, or tissue ingrowth and attachment, among other examples. Thus, these materials potentially find use in a myriad of engineering applications, including medical implants and structural components in the automotive, aerospace, and biomedical industries [1–4]. In particular, synthetic bone scaffolds for osseous tissue regrowth are an area of intense focus and research, in which lightweight porous materials play a crucial role [2,5,6]. Taking inspiration from this application, synthetic bone scaffolds that mimic

---

* Corresponding author.
*E-mail address:* steven.naleway@mech.utah.edu (S.E. Naleway).

https://doi.org/10.1016/j.matdes.2018.107561

**Fig. 1.** Concentric Liesegang rings in sandstone.

cortical bone require a combination of high porosity and specific pore morphology to allow for cell and tissue ingrowth [7]. In addition, cortical bone contains highly ordered structures known as osteons, which exhibit an arrangement of concentric rings separated by lamellar walls, reminiscent of growth rings found in trees and Liesegang rings observed in sedimentary rock [8] (Fig. 1). These naturally occurring concentric rings display varying material properties between adjacent rings, and are in part responsible for the high strength, low density, and high crack propagation resistance of the bulk material [9]. As such, these rings serve as inspiration for fabricating porous materials with this characteristic concentric ring arrangement, and its attendant properties.

Existing techniques for fabricating porous material structures include additive manufacturing [10,11], sacrificial templating and liquid-phase foaming [6,12], and molding fiber- and particle-reinforced polymer matrix composite materials [13]. These techniques have been used in specific applications, including manufacturing biomaterials and impact resistant materials [14–16], but they are limited by material choice, require multiple steps, and/or additional post-processing to create regions of varying material properties within the material structure, and are not easily scalable.

In contrast, freeze casting is an ice-templating technique that enables creating porous scaffolds with a wide range of properties [3,5,17,18]. Freeze casting comprises a four-step process by which porous engineered materials are synthesized through directional freezing of a colloidal slurry containing micro/nano-particles of almost any material [5]. First, a colloidal slurry is prepared that contains solid micro/nano-particles, a liquid freezing agent (e.g., water), polymeric binders, and a dispersant. Second, a freeze front directionally solidifies the colloidal slurry, during which the growth of ice crystals arranges the micro/nano-particles into a porous structure. Third, after freezing, sublimation removes the ice while the solid particles retain their structure, held together by the polymeric binders, resulting in a “green” (i.e., un-sintered) scaffold. Fourth, sintering densifies the green scaffold. After sintering, it is possible to create two-phase composite materials by e.g., infiltrating a two-part epoxy resin into the scaffold. Freeze casting allows tuning several process parameters, and researchers have documented methods to control the pore size, aspect ratio, and lamellar wall thickness of freeze cast scaffolds [4,17,19].

Despite the ability to tune the freeze casting process, one key drawback is the lack of control over the microstructure of the cast materials [4,5]. In its native form, the ice crystal nucleation and growth during freeze casting randomizes the microstructure of the cast materials, which causes variability of the structural and mechanical properties between material samples, even if multiple material samples are cast using the same colloidal slurry and freeze casting process parameters [4,17].

However, several researchers use directed self-assembly (DSA) techniques to control the microstructure of engineered materials fabricated from colloidal slurries [20]. Specifically, external field-based DSA techniques employ e.g., electric, magnetic, or acoustic fields to organize micro/nano-particles dispersed in a liquid medium into user-specified patterns of particles, without constraining the geometry of the resulting material sample. Electric and magnetic field techniques require extremely high field strengths (20.0 kV/m [21] and 80.0 kOe [22], respectively) and, thus, they do not easily scale to cover large areas or volumes, which limits the viability of these techniques to manufacture macroscale material samples. In addition, micro/nano-particles must be electrically conductive and/or ferromagnetic, which restricts material choice. In contrast, ultrasound directed self-assembly allows organizing user-specified patterns of micro/nano-particles dispersed in a liquid medium using the acoustic radiation force associated with a standing ultrasound wave field [23,24]. This technique works independent of the material properties of the micro/nano-particles, and weak attenuation of ultrasound waves in most low-viscosity liquids reduces the need for ultra-high field strengths. The acoustic radiation force associated with the standing ultrasound wave field drives the micro/nano-particles to the nodes or antinodes of the ultrasound wave field, depending on the material properties of the micro/nano-particles and the colloidal slurry [24]. Hence, creating a user-specified pattern of micro/nano-particles requires establishing a standing ultrasound wave field with nodes in locations where micro/nano-particles must aggregate [24].

Thus, the objective of this work is to implement and characterize a fabrication process for macroscale porous engineered material samples with a user-specified microstructure, by combining traditional freeze casting, which allows manufacturing macroscale porous materials samples, with ultrasound DSA, which allows controlling the microstructure of the macroscale porous materials. We refer to this process as “ultrasound freeze casting (UFC),” and employ it to fabricate bioinspired materials that mimic the concentric rings of natural materials such as osteons and Liesegang rings. The standing ultrasound wave field drives micro/nano-particles dispersed in a colloidal slurry into a concentric ring pattern, while the colloidal slurry freezes and fixates the particles into place. After sublimation and sintering, this fabrication process results in a porous material with a user-specified concentric ring microstructure, showing alternating regions of high and low porosity. Thus, using ultrasound DSA in conjunction with the traditional freeze casting process enables materials designers to conveniently implement new materials designs with location specific properties, within a single fabrication process.

## 2. Materials and methods

### 2.1. Ultrasound freeze casting setup

Fig. 2(a) shows the ultrasound freeze casting setup. It consists of a cylindrical piezoelectric (specifically a PZT piezoelectric) ultrasound transducer with a resonant frequency of 1.03 MHz, inner diameter $d_i = 22$ mm and height $h = 20$ mm (APC International, Ltd., Mill Hall, PA, USA), which is used simultaneously as a mold to contain and freeze the colloidal slurry, and to establish an ultrasound standing wave field within the colloidal slurry to assemble the concentric pattern of micro/nano-particles. The cylindrical ultrasound transducer sits on the top surface of a copper cold finger, which is submerged in a reservoir of liquid nitrogen, and creates the temperature gradient and freezing front to solidify the colloidal slurry. A PID temperature controller with a thermocouple and resistive heater regulates the freezing rate of the slurry to 10 °C/min, which was chosen based on past reports that describe creating highly porous, but structurally stable freeze cast materials [17,25]. A 2 mm thick polymer spacer electrically isolates

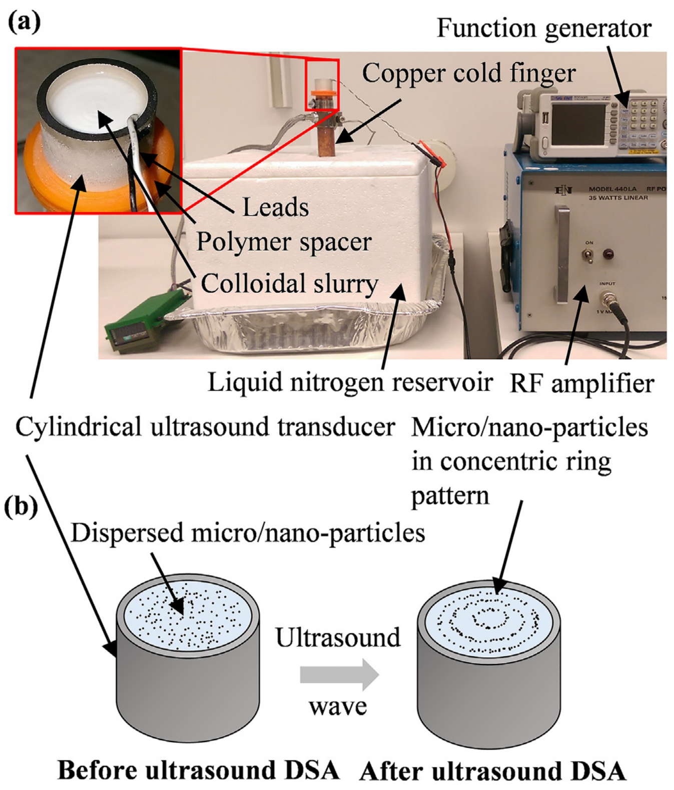

**Fig. 2.** (a) Ultrasound freeze casting set-up, identifying its different components, and (b) schematic of the ultrasound directed self-assembly process creating concentric ring patterns.

the ultrasound transducer from the copper cold finger and resistive heater to avoid electrical short circuits between the power feeding the ultrasound transducer and the freeze casting device, respectively. A function generator (Siglent SDG1025, Siglent Technologies, Solon, OH, USA) and a 45 dB ENI 440LA radio frequency (RF) amplifier drive the ultrasound transducer, causing the micro/nano-particles dispersed in the colloidal slurry to agglomerate at user specific locations, as schematically illustrated in Fig. 2(b).

### 2.2. Material sample fabrication process

A colloidal slurry is prepared by mixing deionized water with 10 vol% of $TiO_2$ particles (< 500 nm diameter, ACROS Organics, Pittsburgh, PA, USA), 1 wt% each of polyethylene glycol (PEG) of 10,000 g/mol (Alfa Aesar, Ward Hill, MA, USA) and polyvinyl alcohol (PVA) of 88,000–97,000 g/mol (Alfa Aesar, Ward Hill, MA, USA) as binder material, and 1 wt% Darvan 811 of 3500 g/mol (R. T. Vanderbilt Company, Inc., Norwalk, CT, USA) as dispersant. 0.22 vol% of 1-Octanol (Sigma-Aldrich, St. Louis, MO, USA) is added to the slurry as an anti-foaming agent. The slurry is mixed in a ball mill with alumina grinding media for 24 h, to obtain a uniformly dispersed slurry, after which it is frozen using the UFC setup of Fig. 2. This slurry composition and mixing procedure is based on prior work of the authors [25,26]. $TiO_2$ particles are selected due to their biocompatibility, which is relevant to biomedical applications. Of note, the same material constituents and mixing processes were used for all slurries, therefore resulting in the same viscosity throughout the process.

Fig. 3(a) shows an isometric view of a cross-section of a typical material sample after freeze casting, with a diameter of 22 mm and a height of 5 mm, whereas Fig. 3(b) shows the top surface of the material sample. Each material sample is fabricated from 7 mL of colloidal slurry and it is freeze cast while driving the ultrasound transducer at operating frequencies of 0 Hz, 650 kHz, 800 kHz and 936 kHz, to obtain material samples with three, four, and five concentric rings of $TiO_2$, respectively. For each of the four operating frequencies, four material samples are fabricated. After freezing, each material sample is freeze dried for 48 h in a freeze dryer (Labconco FreeZone[1], Labconco Corporation, Kansas City, MO, USA) to sublimate the ice, leaving a green scaffold made up of the $TiO_2$ particles, held together by the polymeric binder. Each material sample is subsequently densified via sintering in an open-air furnace (Keith KSK-121700, Keith Company, Pico Rivera, CA, USA) at 925 °C for 3 h (heating and cooling rate of 2 °C/min). Finally, each material sample is vacuum infiltrated with a two-part epoxy resin (Buehler EpoxiCure 2 resin, Buehler, Lake Bluff, IL, USA), and cured in ambient air for 24 h.

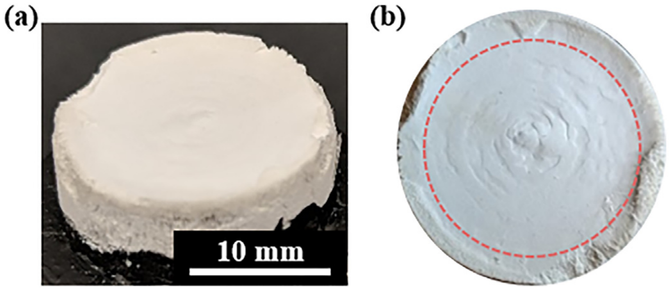

**Fig. 3.** Cross-section of a typical material sample after freeze casting and resin infiltration, showing (a) isometric view, and (b) top view.

Note that, as is commonly done with freeze casting, only the area in the center of the material samples is analyzed in this work, highlighted by the red circle in Fig. 3(b). This is due to surface effects and the temperature gradient that is created close to the external walls of the scaffolds. Thus, the uneven edges seen in Fig. 3 are not included in the sample analysis because they are not representative of the bulk material.

### 2.3. Ultrasound directed self-assembly simulations

Gor'kov's acoustic radiation force theory is used to simulate the locations where $TiO_2$ particles will aggregate within the standing ultrasound wave field established by the cylindrical ultrasound transducer [27]. These locations meet the following three criteria: (1) the acoustic radiation potential $U$ is locally minimum, (2) the acoustic radiation force $\mathbf{f} = -\nabla U$ acting on a spherical $TiO_2$ particle with radius $r_p \ll \lambda$, is almost zero, and (3) it points toward the local minimum of $U$ in the surrounding region. Here, $\lambda = c_m/f$ is the wavelength of the standing ultrasound wave field and $f$ is the corresponding frequency of the ultrasound wave, which propagates in a liquid medium with sound propagation velocity $c_m$ and density $\rho_m$. The ultrasound wave field established by the cylindrical ultrasound transducer primarily propagates in the radial direction and, thus, the time-averaged acoustic radiation potential in polar coordinates $(r, \theta)$ (with origin in the center of the cylindrical ultrasound transducer) is given as [27,28].

$$U = \frac{\pi r_p^3 \overline{p^2}}{3\rho_m c_m^2}\left\{\left(1-\frac{\rho_m c_m^2}{\rho_p c_p^2}\right)J_0^2(kr)-\frac{3\left(\rho_p-\rho_m\right)}{2\rho_p+\rho_m}J_1^2(kr)\right\}, \tag{1}$$

The solution is axisymmetric in the cylindrical transducer and independent of the radial angle $\theta$. $J_o$ and $J_1$ are zero and first order Bessel functions of the first kind, respectively, $k = 2\pi/\lambda$ is the wavenumber, and $\overline{p^2} = p_0^2 J_0(kr)/2$ is the time averaged pressure where $p_0$ is the amplitude of the standing ultrasound wave field. Note that this averaged pressure affects the magnitude of the radiation potential and the corresponding radiation force. Fig. 4 schematically illustrates the radiation potential $U$ within a cylindrical ultrasound transducer, which also serves as a reservoir filled with water and dispersed $TiO_2$ particles. The inset

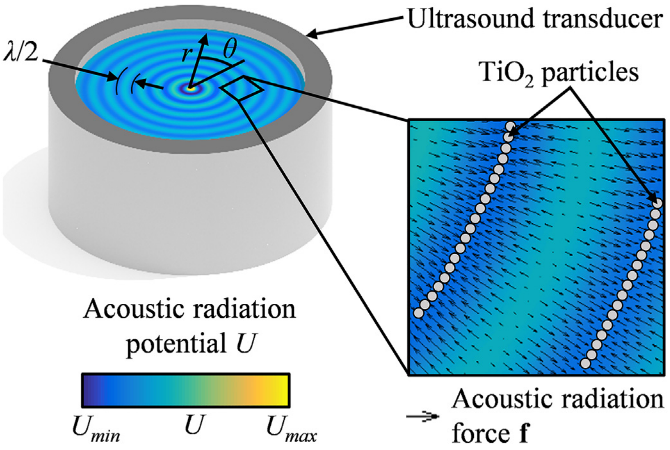

**Fig. 4.** Acoustic radiation potential $U$ within a cylindrical ultrasound transducer, with the inset image showing $TiO_2$ particles aggregated in a concentric pattern.

image shows the acoustic radiation force **f** (black arrows) overlaying the acoustic radiation potential with $TiO_2$ particles aggregating in a concentric ring pattern in the regions where the acoustic radiation potential is locally minimum, and the acoustic radiation force is approximately zero, and points toward particles in the surrounding region. Each concentric ring of $TiO_2$ particles has a radius $n\lambda/2$ where $n \in \mathbb{N} > 0$.

### 2.4. Characterization of the microstructure of the material samples

The top surface of each material sample, where the concentric rings of $TiO_2$ are most visually prominent, are imaged using scanning electron microscopy (SEM) (FEI Quanta 600 FG, Hillsboro, Oregon, USA). In addition, to investigate the effect of the UFC process on the bulk material structure, samples are sectioned through the center of the material sample along the freezing direction, and the transverse cross-sections are imaged. The SEM images are converted into binary images by means of “thresh-holding” using the ImageJ software (National Institutes of Health, Bethesda, MD, USA), assigning a white pixel to a pore (filled with epoxy resin), and a black pixel to a $TiO_2$ particle. From these images, the fraction of pixels that represent a pore quantify porosity in different regions of each material sample. Thus, this method allows mapping the porosity of the top surface of the material samples, and identifying high and low porosity regions, which are referred to in this work as porous and dense regions, respectively. For each material sample, four images are acquired of each of the dense and porous regions, amounting to 128 measurements (16 material samples with 4 images of a porous and 4 images of a dense region per material sample).

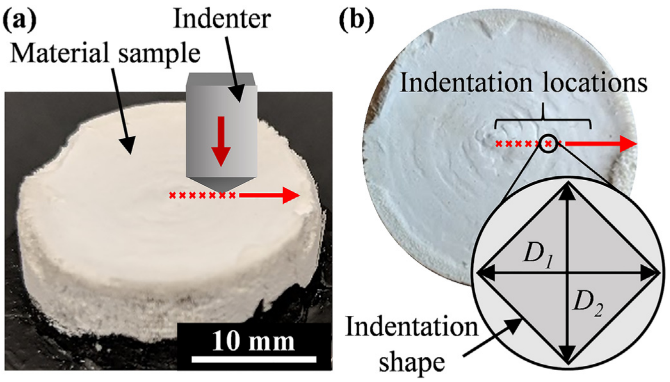

**Fig. 5.** Vickers hardness measurement, showing (a) an isometric view of a typical material sample with indenter, and (b) a top view indicating the different measurement locations, and the characteristic shape of the indentation.

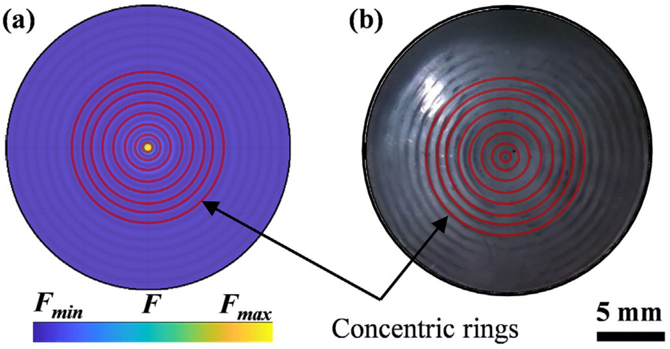

**Fig. 6.** UFC experimental setup validation using 100 nm carbon nanoparticles in water, showing (a) acoustic radiation potential $U$ and (b) experimental results. The red circles accentuate the locations of the concentric rings. (For interpretation of the references to colour in this figure legend, the reader is referred to the web version of this article.)

Note that density in this context refers to the local $TiO_2$ particle and/or material density, not the mass density of the $TiO_2$ that constitutes the scaffold, which is constant in all material samples.

### 2.5. Characterization of the mechanical properties of the material samples

To evaluate the bulk compressive strength of the material samples, uniaxial compression tests parallel to the freezing direction, are performed on 5 × 5 × 5 mm$^3$ sections extracted from each material sample, using an Instron 5967 load frame with a 30 kN load cell. Three samples are tested at each ultrasound operating frequency, i.e., 12 experiments in total. The maximum engineering compressive stress is recorded as the ultimate compressive strength (UCS) and the slope of the engineering compressive stress versus strain in the linear elastic region is recorded as the elastic modulus ($E$).

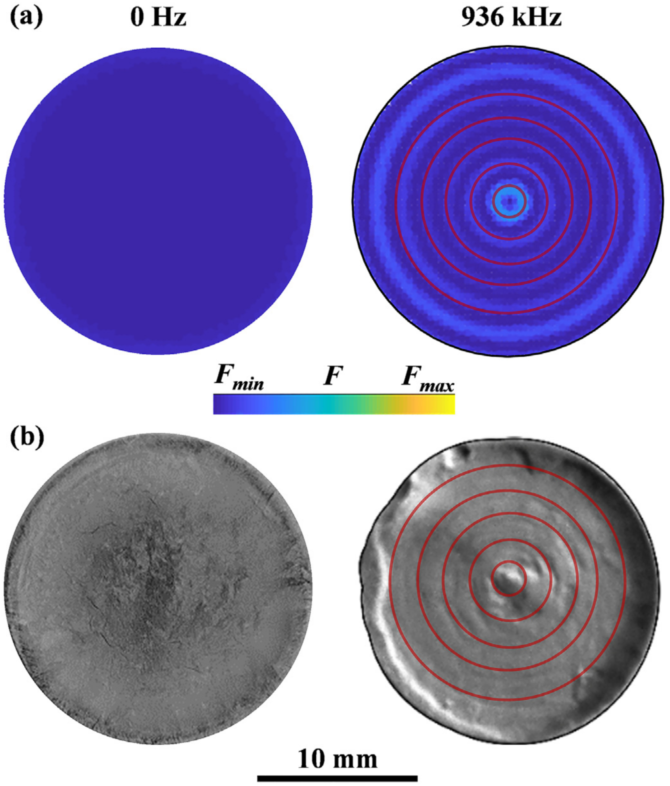

**Fig. 7.** (a) simulated and (b) experimental results of concentric $TiO_2$ rings, showing feasibility of the ultrasound freeze cast fabrication process.

**Table 1**
Porosity and Vickers hardness of material samples fabricated using ultrasound freeze casting, showing different properties for porous and dense regions. The mean values are reported ± one standard deviation.

| Material properties | Ultrasound DSA operating frequency | | |
|---|---|---|---|
| | 0 Hz | 936 kHz | |
| | | Porous | Dense |
| Porosity (%) | 38.51 ± 9.30 | 32.22 ± 5.75 | 21.30 ± 5.81 |
| Vickers hardness | 21.39 ± 6.09 | 19.26 ± 3.29 | 24.51 ± 3.43 |

The Vickers hardness of the top surface of the material samples is measured at 26 equidistant locations along the radius of each material sample, using a microindenter (LECO M400, LECO Corporation, Saint Joseph, MI, USA). This results in 13 indentations within each of the dense and porous regions of each material sample, except in the material samples fabricated with a 0 Hz ultrasound DSA operating frequency, i.e., in which no alternating dense and porous regions exist. Fig. 5 schematically illustrates the Vickers hardness measurements with an isometric view indicating the indenter with respect to the material sample (Fig. 5(a)), and with a top view to schematically depict the different indentation locations (Fig. 5(b)). SEM is used to measure the dimensions $D_1$ and $D_2$ (Fig. 5(b)) of the indentation in the top surface of the material sample to compute the Vickers Hardness (*HV*) as [29].

$$HV = \left(P\frac{1.8544}{1000}\right)\left(0.001\frac{D_1 + D_2}{2}\right)^{-2}, \tag{2}$$

where $P$ is the indentation load applied to the microindenter.

### 2.6. Statistical analysis

The porosity and Vickers hardness measurements of all four material samples fabricated with each ultrasound DSA operating frequency of 0 Hz, 650 kHz, 800 kHz, and 936 kHz, are analyzed via one-way analysis of variance (ANOVA) with $\alpha = 0.05$. For all 16 material samples both the porosity and Vickers hardness are analyzed. Three separate ANOVA analyses are performed. (1) To determine if the UFC process produces consistent results, the porosity and Vickers hardness of the four material samples fabricated with each ultrasound DSA operating frequency are compared to each other. The porous and dense regions are analyzed separately for material samples with non-zero ultrasound operating frequency, which results in 4 porosity measurements and 13 Vickers hardness measurements for each of the dense and porous regions of each of the four material samples fabricated with each of the three non-zero ultrasound operating frequencies, respectively. All measurements are grouped for material samples fabricated with zero ultrasound DSA operating frequency, which results in 8 porosity and 26 Vickers hardness measurements for each of the four material samples. (2) To determine if the designations of dense and porous apply to all material samples, all of the porosity and Vickers hardness measurements of dense and porous regions are grouped. This results in 48 porosity and 156 Vickers hardness measurements for each of the dense and porous regions. (3) To determine if a statistically significant difference exists between the porosity and Vickers hardness of dense and porous regions created by the UFC process with zero and non-zero ultrasound DSA operating frequency, all the porosity and Vickers hardness measurements of the dense and porous regions of material samples fabricated with a non-zero ultrasound DSA operating frequency are grouped, and compared to the porosity and Vickers hardness measurements of the material samples fabricated with zero ultrasound DSA operating frequency. This results in 48 porosity and 156 Vickers hardness measurements for each of the dense and porous regions of material samples fabricated with non-zero ultrasound DSA operating frequency, and 32 porosity and 104 Vickers hardness measurements for the material samples with zero ultrasound DSA operating frequency. When the ANOVA test indicates a statistically significant difference between the material samples fabricated with a non-zero DSA operating frequency, a post-hoc Tukey's honest significant difference (HSD) test for $\alpha = 0.05$ is performed to determine which of the material samples,

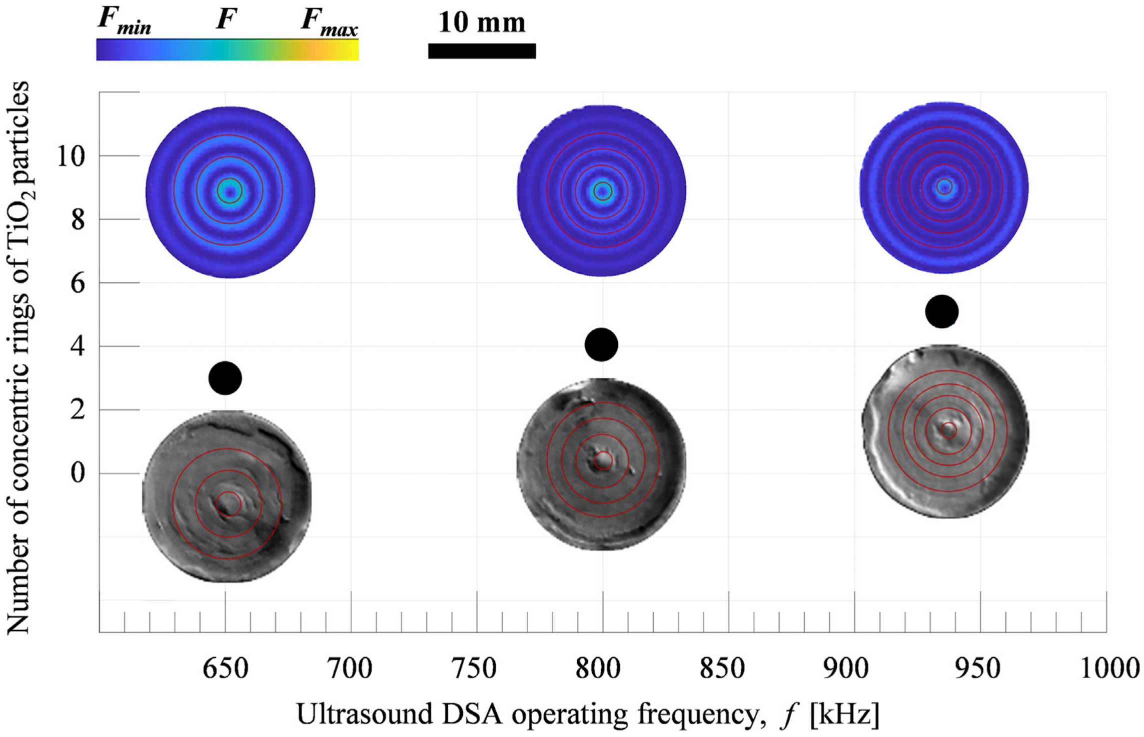

**Fig. 8.** Simulated and experimental results showing the number of concentric $TiO_2$ rings, as a function of ultrasound DSA operating frequency, showing good quantitative agreement.

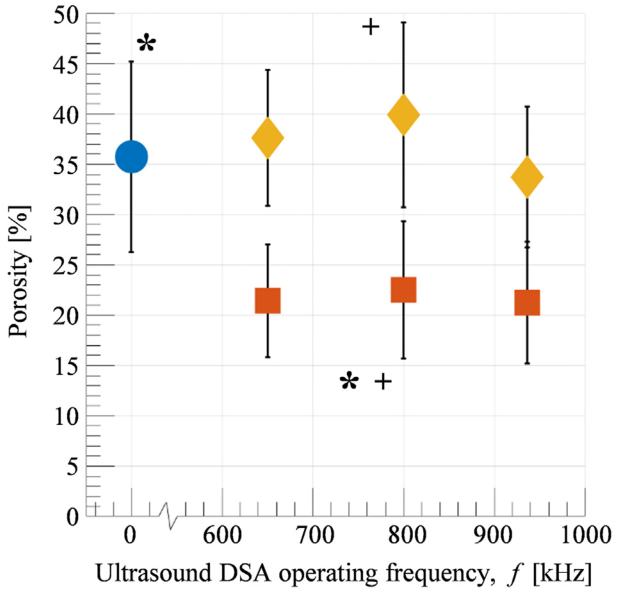

**Fig. 9.** Porosity as a function of ultrasound DSA operating frequency.

fabricated with each ultrasound DSA operating frequency, show statistically significantly different porosity and Vickers hardness.

## 3. Results and discussion

### 3.1. Validation of the ultrasound freeze casting setup

The UFC setup is first validated by organizing carbon nano-particles with an average diameter <100 nm (US Research Nanomaterials, Inc., Houston, TX, USA) dispersed in deionized water, into concentric circles, mimicking a published experiment [23]. Fig. 6 shows a top view of the cylindrical ultrasound transducer and reservoir. Fig. 6(a) displays the ultrasound radiation potential $U$ simulated using Eq. (1), whereas Fig. 6(b) depicts the experimentally obtained aggregation of carbon nanoparticles after ultrasound DSA with a 936 kHz operating frequency (approximately equal to the resonant frequency of the ultrasound transducer). The concentric rings are accentuated with red circles for clarity. Fig. 6 shows the same number of concentric rings for the simulated and experimental results. In addition, the experimental results show good agreement with those of the published experiment [22].

### 3.2. Porosity and mechanical properties of UFC material samples

Fig. 7 illustrates the feasibility of the UFC fabrication process, and shows a comparison of the simulated acoustic radiation potential $U$, predicting the locations of concentric $TiO_2$ rings (Fig. 7(a)), and the experimentally obtained material samples manufactured with an ultrasound DSA operating frequency of 0 and 936 kHz (Fig. 7(b)). The locations of the concentric rings are accentuated using red circles.

From Fig. 7 it is observed that no concentric rings form when the ultrasound field is absent (0 Hz), as expected. The $TiO_2$ are dispersed in the colloidal slurry and do not organize into patterns as no external driving force exists. However, when a standing ultrasound wave field is created with a 936 kHz frequency (approximately equal to the resonant frequency of the ultrasound transducer), the acoustic radiation force drives the $TiO_2$ particles toward the nodes of the standing ultrasound wave pattern, where the acoustic radiation potential $U$ is locally minimum, forming concentric circles in the same locations as predicted by the simulations. Good qualitative agreement is observed between simulated and experimental results.

Table 1 summarizes the porosity and Vickers hardness of dense and porous regions of the material samples fabricated with an ultrasound DSA frequency of 0 Hz and 936 kHz, respectively, obtained using the methods detailed in Section 2, and averaged for all four material samples fabricated with each ultrasound operating frequency.

How well the ultrasound DSA aggregates the $TiO_2$ particles in concentric ring patterns depends on how close the ultrasound operating frequency is to the resonant frequency of the ultrasound transducer. Oftentimes, a PZT ultrasound transducer displays a high quality factor and corresponding non-uniform frequency response function, which causes its displacement amplitude under constant power input to be a function of the ultrasound operating frequency, thus affecting the amplitude of the standing ultrasound created in the reservoir, and potentially the ability to displace and aggregate micro/nano-particles. As such, when studying the effect of ultrasound DSA operating frequency on the UFC

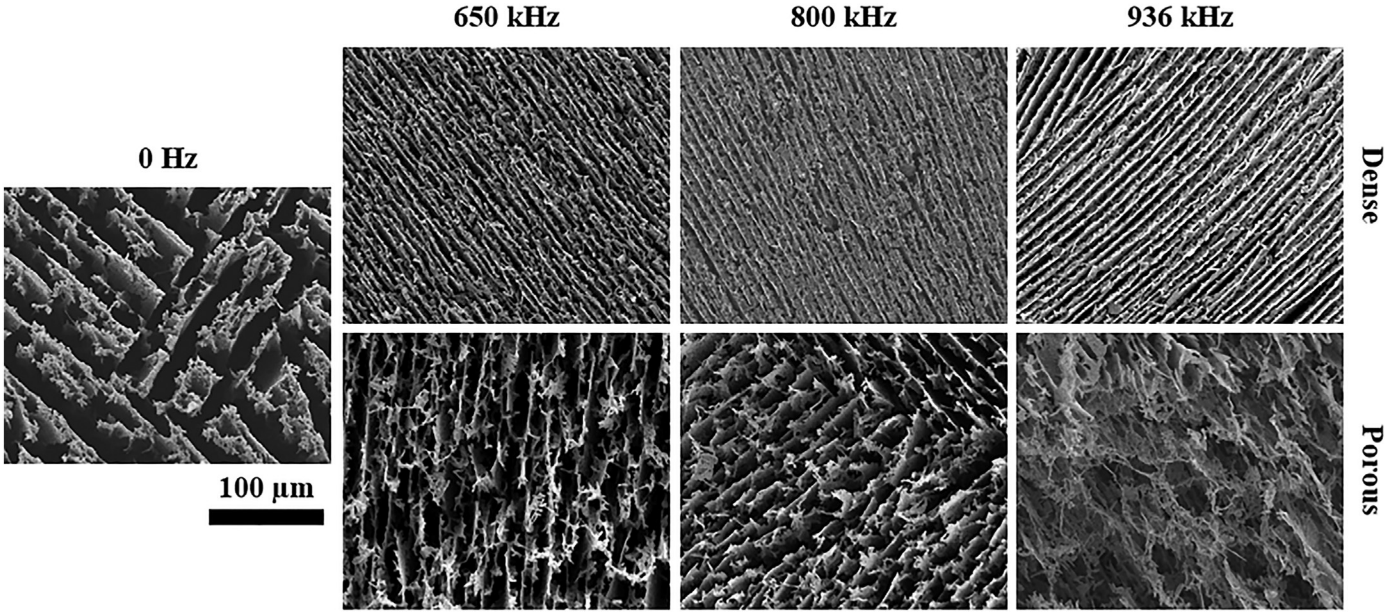

**Fig. 10.** SEM images of dense and porous regions on the surface of the material samples manufactured with each ultrasound operating frequency.

**Table 2**
UCS and *E* of material samples fabricated using ultrasound freeze casting. The mean values are reported ± one standard deviation.

| Material properties | Ultrasound DSA operating frequency | | | |
|---|---|---|---|---|
| | 0 Hz | 650 kHz | 800 kHz | 936 kHz |
| UCS [MPa] | 97.7 ± 7.0 | 96.1 ± 8.2 | 82.1 ± 11.1 | 89.0 ± 13.5 |
| *E* [GPa] | 1.59 ± 0.33 | 1.54 ± 0.32 | 1.26 ± 0.58 | 1.07 ± 0.28 |

process, an ideal experiment requires using ultrasound transducers of identical dimensions but with different resonant frequency. However, this is not practically possible since ultrasound transducer size and resonant frequency are often related. Hence, the effect of ultrasound DSA operating frequency on the UFC process is evaluated using a single ultrasound transducer, with a resonant frequency of 1.03 MHz. It is noted that while ultrasound DSA is best performed near the resonant frequency of the ultrasound transducer, our experiments are able to introduce concentric rings at ultrasound DSA operating frequencies different from the resonant frequency. Fig. 8 shows simulated and experimental results of UFC with $TiO_2$ particles for three different ultrasound DSA operating frequencies. The concentric rings of $TiO_2$ particles are emphasized using red circles. Good quantitative agreement between the simulated and experimentally obtained number of concentric rings is observed.

ANOVA tests do not result in statistically significant differences of porosity and Vickers hardness between the material samples fabricated with the same operating frequency, thus providing evidence that the UFC process fabricates material samples with consistent and repeatable properties. Also, ANOVA tests do not result in statistically significant differences of porosity and Vickers hardness when all dense and porous regions are grouped, thus providing evidence that the dense and porous regions show consistent properties independent of the ultrasound DSA operating frequency.

Fig. 9 shows the porosity as a function of the ultrasound DSA operating frequency, of the dense (red square marker) and porous (orange diamond marker) regions of each material sample, respectively, averaged over all 16 measurements of all material samples. In addition, values for material samples fabricated with 0 Hz ultrasound DSA operating frequency (blue circle marker) are averaged over all 32 measurements of all material samples. The error bars represent one standard deviation. Symbols ("*" and "+") indicate groups of data (i.e., dense and porous regions, along with material samples with 0 Hz ultrasound DSA operating frequency) that display statistically significant differences. The mean porosity of the porous and dense regions of all material samples is 37.08% and 21.73%, respectively. The difference between the porosity of dense and porous regions for material samples manufactured at each operating frequency is 16.18% (650 kHz), 17.37% (800 kHz), and 12.48% (936 kHz), respectively. ANOVA analysis indicates that, when comparing the porosity of dense and porous regions, there is at least one material sample mean that has statistically significant differences from the rest of the data for a 95% confidence level, thus suggesting that the ultrasound DSA resulted in different material properties. A subsequent Tukey's HSD test shows that there are statistically significant differences between the porosity of the dense and porous regions of each material sample ($p < 10^{-6}$), and between the porosity of the dense regions and that of the material samples fabricated with a 0 Hz ultrasound DSA operating frequency ($p < 10^{-6}$). The porosity of the material samples fabricated with 0 Hz ultrasound DSA operating frequency (no concentric rings, blue round marker) do not display a statistically significant difference with that of the porous concentric rings in the material samples fabricated with an ultrasound DSA operating frequency of 650 kHz and 936 kHz, respectively. This is likely due to the slurry below the free top surface acting as a reservoir of $TiO_2$ particles, maintaining constant $TiO_2$ particle concentration in the porous region, as particles are displaced to the nodes of the standing ultrasound wave. It may also be due to the advancement of the freeze front within the slurry, which could displace $TiO_2$ particles that migrate upwards toward the free surface of the material sample [1,30].

Fig. 10 shows SEM images of the dense and porous regions on the surfaces of the material samples manufactured with each ultrasound operating frequency. Images are shown for the sample with no applied ultrasound DSA operating frequency (0 Hz) and the dense and porous regions of material samples fabricated with applied ultrasound DSA operating frequencies of 650, 800, and 936 kHz. In agreement with the

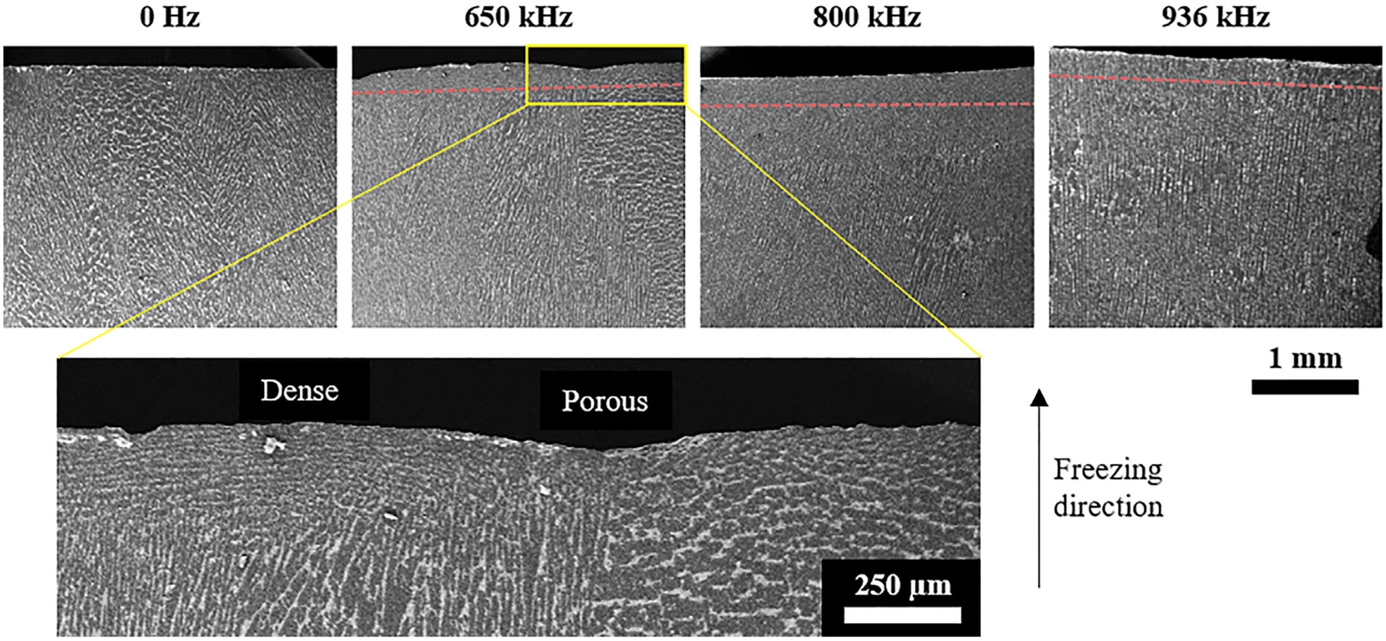

**Fig. 11.** Representative longitudinal cross-sections (in the freezing direction) imaged with SEM at each applied ultrasound DSA operating frequency. It can be seen that ordering only occurs in the 0.5–1 mm at the top of the sample, as highlighted by red dashed lines. The inset shows this region for a sample created with an applied ultrasound DSA operating frequency of 650 kHz where the dense and porous regions can be seen in the longitudinal cross section. (For interpretation of the references to colour in this figure legend, the reader is referred to the web version of this article.)

results shown in Fig. 9, it can be seen that the microstructure obtained at with 0 Hz (no ultrasound exposure) is similar to the porous regions of samples fabricated with an applied non-zero ultrasound DSA operating frequency.

Table 2 shows the UCS, and $E$ of the material samples manufactured with each of ultrasound operating frequencies. ANOVA analysis showed no statistically significant differences between the UCS ($p = 0.45$) and $E$ ($p = 0.36$) for different ultrasound operating frequencies.

To clarify the results shown in Table 2, Fig. 11 shows SEM images of the longitudinal cross-sections (in the freezing direction) of the material samples manufactured with each of the ultrasound operating frequencies, and infiltrated with an epoxy prior to imaging to improve image clarity. Fig. 11 shows that, while dense and porous regions are highly visible in the microstructure at the surface of the samples, they only extend 0.5–1 mm into the depth of the sample (as highlighted by red dashed lines), as evidenced by the change in microstructure that occurs at that depth. The inset image provides greater detail for a sample created with an ultrasound DSA operating frequency of 650 kHz, and shows that the lamellar walls are reoriented by the ultrasound DSA into the dense and porous regions.

Fig. 12(a) shows the Vickers hardness as a function of the ultrasound DSA operating frequency, of the dense (red square marker) and porous (orange diamond marker) regions of each material sample, respectively, along with material samples fabricated with a 0 Hz ultrasound DSA operating frequency. The results are averaged over all measurements of all material samples, and the error bars represent one standard deviation. The Vickers hardness increases with decreasing porosity, as expected (Figs. 9 and 10 combined). The mean Vickers hardness of the porous and dense regions of all material samples is 19.37 HV and 24.52 HV, respectively. The difference of mean Vickers hardness between dense and porous regions for material samples fabricated with each operating frequency is 5.47 HV (650 kHz), 4.72 HV (800 kHz), and 5.25 HV (936 kHz), respectively. Material samples fabricated with no concentric rings of $TiO_2$ particles display a mean Vickers hardness of 21.40 HV (blue circular marker), with a standard deviation of 6.09 HV. The ANOVA and Tukey's HSD results ($\alpha = 0.05$) indicate that there are statistically significant differences between the Vickers hardness of dense and porous regions of all material samples ($p < 10^{-6}$), and between the Vickers hardness of the material samples fabricated with 0 Hz ultrasound DSA operating frequency, and the Vickers hardness of the dense and porous regions of each material sample fabricated with non-zero ultrasound DSA frequency ($p < 10^{-6}$ and $p = 0.012$, respectively), thus suggesting that the ultrasound DSA resulted in different mechanical properties. This result is different from that obtained with porosity measurements, in which the porosity of the porous region and that of the material samples fabricated with 0 Hz ultrasound DSA operating frequency did not display a statistically significant difference. In addition, a representative SEM image of an indent is displayed in Fig. 12(b), which shows a clean indent free of pullout or brittle fracture.

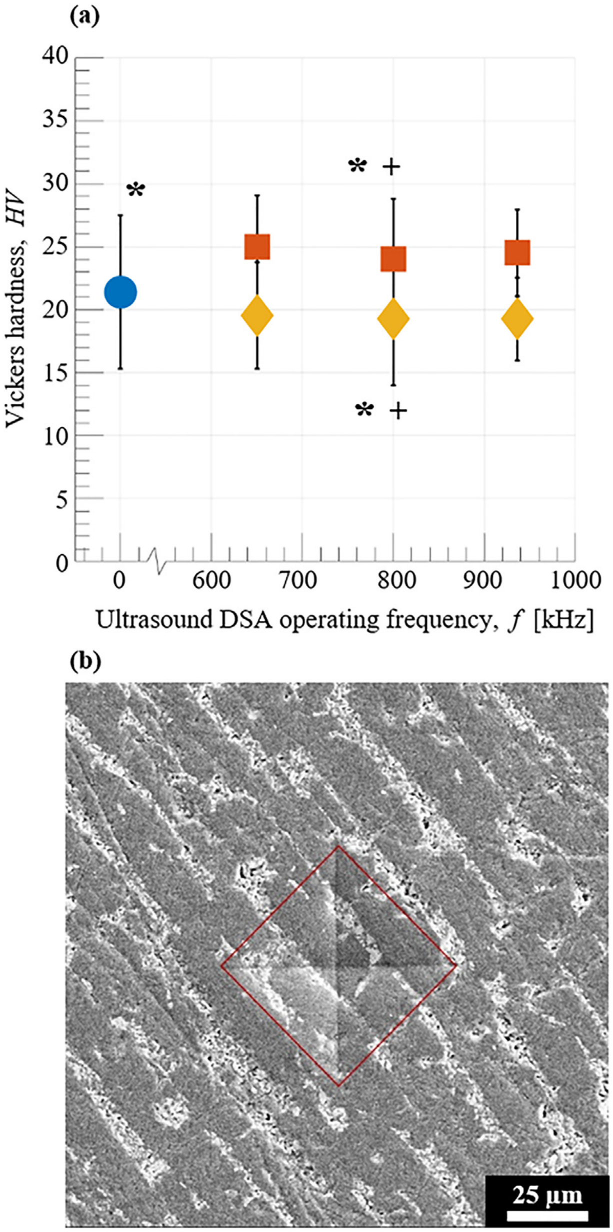

**Fig. 12.** (a) Vickers hardness as a function of ultrasound DSA operating frequency, and (b) a representative SEM image of an indentation in the epoxy-infiltrated material sample, which displayed a clean indent, free of brittle fracture.

To further illustrate the local Vickers hardness in a typical material specimen (ultrasound DSA operating frequency = 650 kHz), Fig. 13 (a) shows the Vickers hardness as a function of the radial coordinate from the center to the edge of a material sample. The Vickers hardness measurements are superimposed onto the simulated acoustic radiation force results, indicating how the simulated regions where $TiO_2$ particles accumulate, map to regions of high Vickers hardness, and vice versa. This depicts how porosity and Vickers hardness changes between dense and porous regions of the material sample. Fig. 13(b) shows an SEM image of a typical material sample fabricated with an ultrasound DSA operating frequency of 650 kHz to illustrate that the concentric rings of $TiO_2$ display a marked difference in material density, shown as a greyscale gradient in the image, with darkness increasing with decreasing density.

Using a standing ultrasound wave field to obtain control over the microstructure of a freeze cast scaffold through ultrasound DSA contrasts existing techniques that require intrinsic changes to the composition of the colloidal slurry to alter the microstructure of the scaffold [4,17]. As such, UFC enables creating bioinspired concentric rings within a porous $TiO_2$ scaffold using a single fabrication process. These concentric rings contain regions of varying material properties (i.e., dense and porous rings), which differs from previous techniques that require multiple processes to achieve a similar effect [19,31,32]. The number of concentric rings is controlled by changing the operating frequency of the standing ultrasound wave field, and is limited by the frequency response function of the ultrasound transducer, the transducer material properties, and the available input power to the transducer. Hence, UFC offers the ability to tailor material properties in specific, user-specified locations of the bulk material. This, in turn, allows fabricating bulk materials with (material and mechanical) properties that depend on location in the material, which could find use in a myriad of engineering applications. This work shows the ability to tailor the number of concentric rings and, thus, create porous and dense regions with consistent properties, throughout the bulk material.

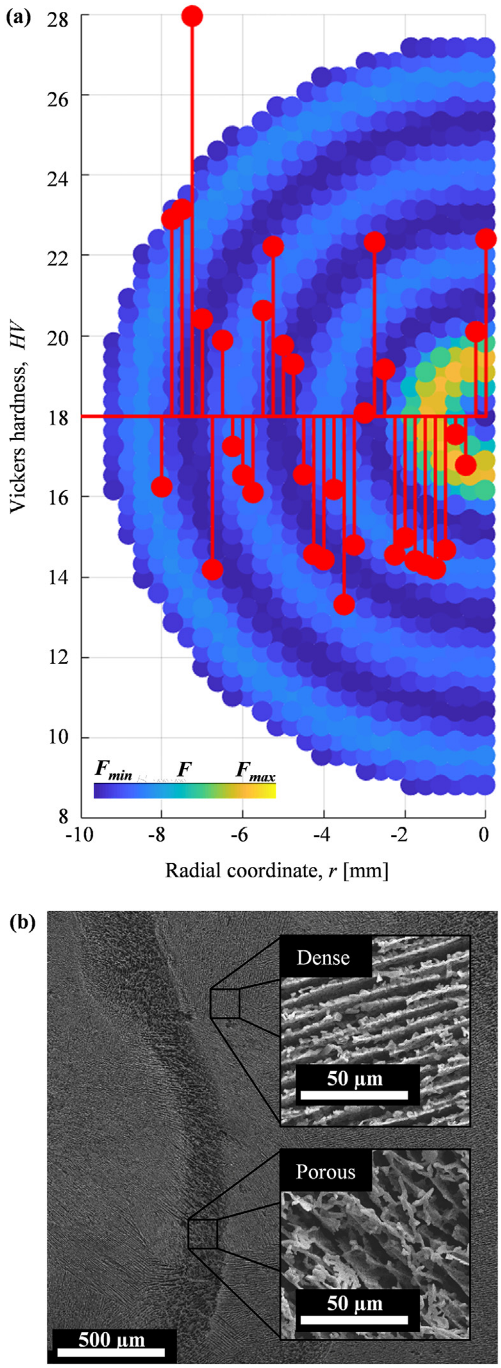

**Fig. 13.** (a) Vickers hardness as a function of radial coordinate for a typical material sample, fabricated using an ultrasound DSA operating frequency of 650 kHz, and (b) SEM images showing dense and porous regions of the material sample.

Both freeze casting and ultrasound DSA are processes that, in theory, can be used in conjunction with any material chemistry (e.g., polymers, ceramics, and metals). However, there are known limitations to both processes in terms of the particle size that can be employed due to the attenuation of pressure waves (in terms of ultrasound DSA) and the dispersion of particles in a colloidal solution (in terms of freeze casting). In addition, a limitation of the current UFC process is that the features are most prominent at the surface of the sample due to the dynamic freezing process and therefore the bulk compressive properties are not impacted. While it may be possible to achieve features that extend throughout the entire structure, it is beyond the scope of this current work.

Despite these limitations, this work lays the framework for a fabrication method for ceramic materials with a diversity of microstructures and mechanical properties using a single fabrication process. In addition, it could be employed to enhance to recently reported techniques in metal-based [33,34], bioinspired [35], piezoelectric-based [36], and biocompatible [37,38] freeze casting. This improves upon the state-of-the-art, where these properties are only available through the use of multiple processing steps. Of importance, we show that these properties can be tailored by altering the applied ultrasound DSA operating frequency, allowing for user-specific designs that can be employed in a variety of applications. For example, it is well known that cells will preferentially grow based upon the microstructure of their substrate. Future applications could target cell growth into specific areas of material created with the UFC process to incorporate targeted microstructures that would influence the growth of cells in vitro or in vivo and, therefore improve the overall biocompatibility of these materials.

## 4. Conclusion

An ultrasound freeze casting process is implemented and used to fabricate bioinspired materials with porous concentric $TiO_2$ rings that mimic the structure of naturally occurring materials, including osteons in cortical bone and the geological formations knows as Liesegang rings found in sedimentary rock. The concentric rings display alternating regions of high and low porosity and Vickers hardness, and the number of rings is controlled by the operating frequency of the ultrasound transducer.

The porosity difference between alternating porous and dense regions is statistically significant ($p < 10^{-6}$), with a mean porosity of 37.08% and 21.73% for the porous and dense regions, respectively. A statistically significant difference also exists between the porosity of the dense regions of the $TiO_2$ scaffolds and the porosity of the material samples with no rings ($p < 10^{-6}$).

The Vickers hardness difference between alternating porous and dense regions is statistically significant, as well as between the dense regions and the material samples without concentric $TiO_2$ rings. The mean Vickers hardness for the dense and porous regions is 24.52 HV and 19.37 HV ($p < 10^{-6}$). The mean Vickers hardness of the material samples without concentric rings is 21.40 HV, which is statistically different from both the dense ($p < 10^{-6}$) and porous regions ($p < 0.012$) of the material samples with concentric $TiO_2$ rings.

## Data availability

The raw data required to reproduce these findings are available to download from https://bioinspired.mech.utah.edu/. The processed data required to reproduce these findings are available to download from https://bioinspired.mech.utah.edu/.

## CRediT authorship contribution statement

**Taylor A. Ogden:** Data curation, Formal analysis, Investigation, Writing - original draft, Visualization. **Milo Prisbrey:** Data curation, Formal analysis, Investigation, Writing - original draft, Visualization. **Isaac Nelson:** Data curation, Formal analysis, Investigation, Writing - original draft, Visualization. **Bart Raeymaekers:** Formal analysis, Funding acquisition, Project administration, Resources, Visualization, Writing - original draft, Writing - review & editing. **Steven E. Naleway:** Formal analysis, Funding acquisition, Project administration, Resources, Visualization, Writing - original draft, Writing - review & editing.

## Acknowledgements

This work was financially supported by the National Science Foundation under grant CMMI #1660979. The authors wish to thank Dr. Krista Carlson and Dr. Sivaraman Guruswamy for their help with performing the Vickers hardness testing.

## References

[1] S. Deville, E. Saiz, R.K. Nalla, A.P. Tomsia, Freezing as a path to build complex composites, Science 311 (2006) 515–518.

[2] E. Munch, M.E. Launey, D.H. Alsem, E. Saiz, A.P. Tomsia, R.O. Ritchie, Tough, bio-inspired hybrid materials, Science 322 (2008) 1516–1520.

[3] M.M. Porter, J. Mckittrick, M.A. Meyers, Biomimetic materials by freeze casting, JOM 65 (2013) 720–727.

[4] M.M. Porter, R. Imperio, M. Wen, M.A. Meyers, J. McKittrick, Bioinspired scaffolds with varying pore architectures and mechanical properties, Adv. Funct. Mater. 24 (2014) 1978–1987.

[5] S. Deville, E. Saiz, A.P. Tomsia, Freeze casting of hydroxyapatite scaffolds for bone tissue engineering, Biomaterials 27 (2006) 5480–5489.

[6] A. Tampieri, S. Sprio, A. Ruffini, G. Celotti, I.G. Lesci, N. Roveri, From wood to bone: multi-step process to convert wood hierarchical structures into biomimetic hydroxyapatite scaffolds for bone tissue engineering, J. Mater. Chem. 19 (2009) 4973–4980.

[7] S. Weiner, H.D. Wagner, The material bone: structure mechanical function relations, Annu. Rev. Mater. Sci. 28 (1998) 271–298.

[8] L. Fu, K.L. Milliken, J.M. Sharp, Porosity and permeability variations in fractured and Liesegang-Banded Breathitt sandstones (Middle Pennsylvanian), eastern Kentucky - diagenetic controls and implications for modeling dual-porosity systems, J. Hydrol. 154 (1994) 351–381.

[9] M.E. Launey, M.J. Buehler, R.O. Ritchie, On the mechanistic origins of toughness in bone, Annu. Rev. Mater. Sci. 40 (2010) 25–53.

[10] B.G. Compton, J.A. Lewis, 3D-printing of lightweight cellular composites, Adv. Mater. 26 (2014) 5930–5935.

[11] C. Zhu, T.Y.J. Han, E.B. Duoss, A.M. Golobic, J.D. Kuntz, C.M. Spadaccini, M.A. Worsley, Highly compressible 3D periodic graphene aerogel microlattices, Nat. Commun. 6 (2015) 6962.

[12] P. Colombo, Conventional and novel processing methods for cellular ceramics, Phil. Trans. R. Soc. A 364 (2006) 109–124.

[13] L.K. Grunenfelder, N. Suksangpanya, C. Salinas, G. Milliron, N. Yaraghi, S. Herrera, K. Evans-Lutterodt, S.R. Nutt, P. Zavattieri, D. Kisailus, Bio-inspired impact-resistant composites, Acta Biomater. 10 (2014) 3997–4008.

[14] A. Butscher, M. Bohner, S. Hofmann, L. Gauckler, R. Muller, Structural and material approaches to bone tissue engineering in powder-based three-dimensional printing, Acta Biomater. 7 (2011) 907–920.

[15] S.M. Peltola, F.P.W. Melchels, D.W. Grijpma, M. Kellomaki, A review of rapid prototyping techniques for tissue engineering purposes, Ann. Med. 40 (2008) 268–280.

[16] H.N.G. Wadley, Multifunctional periodic cellular metals, Phil. Trans. R. Soc. A 364 (2006) 31–68.

[17] S.E. Naleway, C.F. Yu, R.L. Hsiong, A. Sengupta, P.M. Iovine, J.A. Hildebrand, M.A. Meyers, J. McKittrick, Bioinspired intrinsic control of freeze cast composites: harnessing hydrophobic hydration and clathrate hydrates, Acta Mater. 114 (2016) 67–79.

[18] H. Lee, T.S. Jang, J. Song, H.E. Kim, H.D. Jung, The production of porous hydroxyapatite scaffolds with graded porosity by sequential freeze-casting, Materials 10 (2017), E367.

[19] M.M. Porter, P. Niksiar, J. McKittrick, Microstructural control of colloidal-based ceramics by directional solidification under weak magnetic fields, J. Am. Ceram. Soc. 99 (2016) 1917–1926.

[20] M. Grzelczak, J. Vermant, E.M. Furst, L.M. Liz-Marzan, Directed self-assembly of nanoparticles, ACS Nano 4 (2010) 3591–3605.

[21] P.V. Kamat, K.G. Thomas, S. Barazzouk, G. Girishkumar, K. Vinodgopal, D. Meisel, Self-assembled linear bundles of single wall carbon nanotubes and their alignment and deposition as a film in a DC field, J. Am. Chem. Soc. 126 (2004) 10757–10762.

[22] M. Fujiwara, E. Oki, M. Hamada, Y. Tanimoto, I. Mukouda, Y. Shimomura, Magnetic orientation and magnetic properties of a single carbon nanotube, J. Phys. Chem. A 105 (2001) 4383–4386.

[23] B. Raeymaekers, C. Pantea, D.N. Sinha, Manipulation of diamond nanoparticles using bulk acoustic waves, J. Appl. Phys. 109 (2011), 014317.

[24] J. Greenhall, F.G. Vasquez, B. Raeymaekers, Ultrasound directed self-assembly of user-specified patterns of nanoparticles dispersed in a fluid medium, Appl. Phys. Lett. 108 (2016), 103103.

[25] S.E. Naleway, C.F. Yu, M.M. Porter, A. Sengupta, P.M. Iovine, M.A. Meyers, J. McKittrick, Bioinspired composites from freeze casting with clathrate hydrates, Mater. Des. 71 (2015) 62–67.

[26] S.E. Naleway, K.C. Fickas, Y.N. Maker, M.A. Meyers, J. McKittrick, Reproducibility of $ZrO_2$-based freeze casting for biomaterials, Mater. Sci. Eng. C 61 (2016) 105–112.

[27] M. Barmatz, P. Collas, Acoustic radiation potential on a sphere in plane, cylindrical, and spherical standing wave fields, J. Acoust. Soc. Am. 77 (1985) 928–945.

[28] E.G. Lierke, Deformation and displacement of liquid drops in an optimized acoustic standing wave levitator, Acta Acust. Acust. 88 (2002) 206–217.

[29] ASTM Standard E384, Standard Test Method for Microindentation Hardness of Materials, ASTM International, West Conshohocken, PA, USA, 2017, https://doi.org/10.1520/E0384-1517www.astm.org.

[30] J.Z. Zhao, Y. Li, Y. Wu, S.S. Lv, K. Lu, Microstructure of $TiO_2$ porous ceramics by freeze casting of nanoparticle suspensions, Ceram. Int. 43 (2017) 14593–14598.

[31] M.M. Porter, L. Meraz, A. Calderon, H.J. Choi, A. Chouhan, L. Wang, M.A. Meyers, J. McKittrick, Torsional properties of helix-reinforced composites fabricated by magnetic freeze casting, Compos. Struct. 119 (2015) 174–184.

[32] M.B. Frank, S.H. Siu, K. Karandikar, C.H. Liu, S.E. Naleway, M.M. Porter, O.A. Graeve, J. McKittrick, Synergistic structures from magnetic freeze casting with surface magnetized alumina particles and platelets, J. Mech. Behav. Biomed. Mater. 76 (2017) 153–163.

[33] S.K. Wilke, D.C. Dunand, Structural evolution of directionally freeze-cast iron foams during oxidation/reduction cycles, Acta Mater. 162 (2019) 90–102.

[34] J. Gubicza, R. Nemeth, H. Park, K. Kim, J.H. Kim, M. Ovari, M. Mohai, H. Choe, Effect of lithiation on the microstructure of a cobalt foam processed by freeze casting, Adv. Eng. Mater. 20 (2018), 1800343.

[35] S. Askarinejad, N. Rahbar, Mechanics of bioinspired lamellar structured ceramic/polymer composites: experiments and models, Int. J. Plast. 107 (2018) 122–149.

[36] J.I. Roscow, Y. Zhang, M.J. Krasny, R.W.C. Lewis, J. Taylor, C.R. Bowen, Freeze cast porous barium titanate for enhanced piezoelectric energy harvesting, J. Phys. D 51 (2018), 225301.

[37] G. Singh, S. Soundarapandian, Effect of freezing conditions on beta-tricalcium phosphate/camphene scaffold with micro sized particles fabricated by freeze casting, J. Mech. Behavior Biomed. Mats. 79 (2018) 189–194.

[38] Z.Q. Jia, Z.X. Guo, F. Chen, J.J. Li, L. Zhao, L. Zhang, Microstructure, phase compositions and in vitro evaluation of freeze casting hydroxyapatite-silica scaffolds, Ceram. Int. 44 (2018) 3636–3643.